

Ductile to brittle transition of $\text{Cu}_{46}\text{Zr}_{47}\text{Al}_7$ metallic glass composites

J.T. Fan^a, Z.F. Zhang^{a,*}, F. Jiang^b, J. Sun^b, S.X. Mao^{a,c}

^a Shenyang National Laboratory for Materials Science, Institute of Metal Research, The Chinese Academy of Science, Shenyang 110016, People's Republic of China

^b State Key Laboratory for Mechanical Behavior of Materials, Xi'an Jiaotong University, Xi'an 710049, People's Republic of China

^c Department of Mechanical Engineering, University of Pittsburgh, Pittsburgh, PA 15261, USA

Received 1 August 2007; received in revised form 30 September 2007; accepted 16 October 2007

Abstract

The ductile to brittle transition behaviors of $\text{Cu}_{46}\text{Zr}_{47}\text{Al}_7$ metallic glass and its composite with different microstructures were systematically evaluated by Vickers hardness and small punch test, on the base of the uniaxial compression properties reported before. It was found that the metallic glass composite containing different volume fraction of primary crystallization phases displayed a transition from ductility to brittleness, which can be well revealed by both the Vickers hardness and the small punch tests. For example, the number of shear bands appearing around the indentation of Vickers hardness trends to decrease with the increase in the volume fraction of primary crystallization phases in the metallic glass composites. After small punch tests, the shear deformation and failure behaviors were also found to display obvious ductile to brittle transition. And even the small punch test can distinguish the difference in their intrinsic shear deformation ability more delicately. Based on the experimental results above, the ductile to brittle transition in the metallic glass composite was discussed.

© 2007 Elsevier B.V. All rights reserved.

Keywords: Metallic glass; Shear bands; Ductility; Brittleness; Small punch test

1. Introduction

Bulk metallic glasses (BMGs) have been found in many alloy systems, which has attracted tremendous attention since their first emergence about 40 years ago [1–5]. At the same time, they also offer unique potential as structural materials for high strength, high hardness, good wear and corrosion resistance [6,7]. Unfortunately, these properties cannot be fully exploited in monolithic amorphous metals due to the lack of plasticity in unconfined loading geometries. In order to improve the plasticity, many investigations have been carried out by introducing a reinforcing phase into the BMG matrix, which introduces a new kind of material, the BMG matrix composite [8,9]. Recently, it is interesting to find that the Zr–Cu–Al ternary alloys have a better combination of high strength, good ductility and lower production cost, compared with the other BMG alloys [10–12]. It was reported that $\text{Cu}_{47.5}\text{Zr}_{47.5}\text{Al}_5$ BMG exhibited sound “work hardening” and large plastic strain of 18% together with a high-compressive strength of up to 2265 MPa [13]. Besides,

plasticity-improved Zr–Cu–Al BMG matrix composites were also fabricated with many martensite phases [14]. However, the small size, seldom larger than 4 mm in diameter, limits its application as structural materials. To reveal the deformation and fracture mechanism of metallic glasses and their composites, the conventional experimental tests, for example uniaxial compression, tension, bending and so on, were always employed [5,15]. It is widely observed that metallic glasses often exhibit brittle fracture under tension, and different plasticity under compression [5,12–17]. This gives rise to an interesting question: whether one can find some novel testing method to further reveal the difference in the deformation and fracture mechanisms of different metallic glasses and their composites?

In this paper, a $\text{Cu}_{46}\text{Zr}_{47}\text{Al}_7$ alloy was cast into wedge shape with thickness up to 9 mm. The different thickness of the bulk samples led to varying cooling rates upon solidification, and furthermore resulted in different microstructures and volume fraction of primary crystallization phases. Therefore, it is convenient to compare the transition in the mechanical properties and the corresponding deformation and fracture mechanism. For better understanding such transition, besides the conventional Vickers hardness tests, we employed a new test method, i.e., small punch test, to further reveal the difference in the

* Corresponding author.

E-mail address: zhfzhang@imr.ac.cn (Z.F. Zhang).

deformation and fracture mechanism of the metallic glass composites, and the results were also compared with that of Vickers hardness and reported uniaxial compressive test.

2. Experimental procedure

In the present work, the alloy ingot, with a nominal composition of $\text{Cu}_{46}\text{Zr}_{47}\text{Al}_7$ (at.%), was prepared by arc melting mixture of ultrasonically cleansed Zr (crystal bar, 99.9 at.%), Cu (99.99 at.%) and Al (99.99 at.%) pieces in a Ti-gettered high-purity argon atmosphere. Besides, the electromagnetic stirring function was introduced to the equipment in order to make the elements more homogeneous [16]. Each ingot was re-melted at least four times, and then was cast into a wedge-shaped plate with a dimension of $90\text{ mm} \times 30\text{ mm} \times T\text{ mm}$ (T is from 2 to 9) by copper mold casting method. Four groups of samples were cut from the center of cross-section at four different positions with the thicknesses of 2, 4, 6 and 8 mm, defined as samples A–D, respectively (Fig. 1). The Vickers hardness tests with the load of 200 g for 10 s were carried out with MVK-H3 tester on the metallic glass sample surface after carefully polished, and then the results were averaged as the Vickers hardness. Besides, the small punch test was carried out by the small device, as illustrated in Fig. 2. This test requires the specimen in a small disk with a diameter larger than 3 mm and a thickness of 0.1 mm, which is clamped over a circular guide hole with 1 mm in diame-

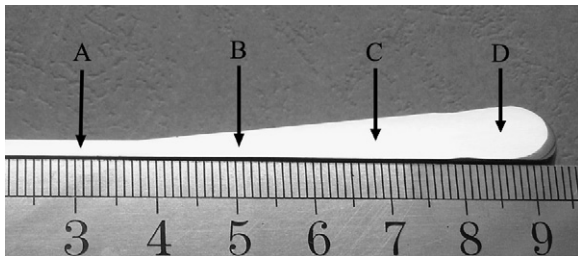


Fig. 1. Optical photo about the wedge-shaped plate of the as-cast $\text{Cu}_{46}\text{Zr}_{47}\text{Al}_7$ alloy designated samples A–D.

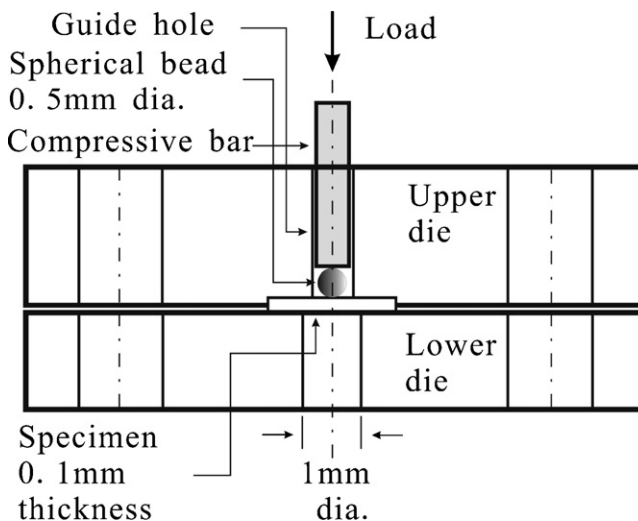


Fig. 2. Sketch of experimental setup for the small punch test.

ter between the two rigid dies. The specimen was then subjected to a lateral indenter driven at a constant load by the compression bar through the guide hole. The tip of the compression bar is spherical bead, made from hard carbide with 0.5 mm in diameter, which contacts with the sample straightly. Finally, all the deformation and fracture morphologies were observed by using a Quanta-600 scanning electron microscopy (SEM).

3. Results and discussion

3.1. Microstructures and mechanical properties

We have reported the microstructures change with the increase in the thickness or the cooling rate [18]. The X-ray diffraction (XRD) shows that the microstructure of sample A is fully amorphous glass. However, for samples B and C, the visible crystalline diffraction peaks were detected as CuZr and $\text{Cu}_{10}\text{Zr}_7$, only with the different intensity. For sample D, besides the left CuZr phase, another new diffraction peak was detected as Zr_2Cu . Besides, based on the DSC data, the volume fractions of the crystallization phases were estimated according to the method reported by Bian et al. [19]:

$$V_{\text{crys}}(\%) = \frac{\Delta H_{\text{max}} - \Delta H}{\Delta H_{\text{max}}} \quad (1)$$

where ΔH_{max} is the total enthalpy of transformation from the fully amorphous alloy to the completely crystallized alloy and ΔH is the enthalpy of the tested samples. Consequentially, the volume fractions of primary crystallization phases are about 0%, 29%, 95% and 100%, for samples A–D, respectively. In addition, we have also reported the compressive engineering stress–strain curves of samples A–D [18]. For sample A, its fracture strength, σ_f and plastic strain, ε_p are about 2.06 GPa and 14.5%. For sample B, its fracture strength and plastic strain, ε_p are about 1.92 GPa and 4.4%. For samples C and D, they only displayed elastic deformation and then catastrophically failed with a zero plastic strain with fracture strength of about 1.07 GPa and 1.03 GPa. Visibly, the compressive properties become deteriorating gradually with the increase in volume fraction of primary crystallization phases, although the fully amorphous alloy can display quite high strength and good plastic deformation ability.

In this work, the values of Vickers hardness, H_V were measured, and are equal to 5.8, 5.7, 5.4 and 3.9 GPa, respectively for samples A, B, C, and D, with a decreasing order too. All the mechanical properties are listed in Table 1. Clearly, the mechanical properties are sensitive to the microstructures and change of crystallization phases. Thus one can compare the relationships of thickness versus strength, plastic strain, and Vickers hardness, as plotted in Fig. 3. Visibly, the strength, plasticity and hardness decrease with the increase in thickness, due to the change in volume fraction of primary crystallization phases. For sample B, the calculated volume fraction of the primary crystallization phases is about 29%, however, its hardness and strength only decrease very slightly compared with those of sample A. This indicates that even though the Zr–Cu–Al metallic glass composite contains some primary crystallization phases, it can still exhibit high hardness and strength, due to the main effect of

Table 1
Summary of microstructures and mechanical properties of $\text{Cu}_{46}\text{Zr}_{47}\text{Al}_7$ alloys designated as samples A–D [18]

Sample	T (mm)	H_V (GPa)	σ_f (GPa)	ε_p (%)	V_{cryst} (%)	Structure
A	2.3	5.8	1.99	14.5	0	Fully glass
B	4.2	5.7	1.92	4.4	29	Glass + CuZr + Cu_{10}Zr
C	6.4	5.4	1.07	–	95	Glass + CuZr + $\text{Cu}_{10}\text{Zr}_7$
D	8.3	3.9	1.03	–	100	CuZr + Zr_2Cu

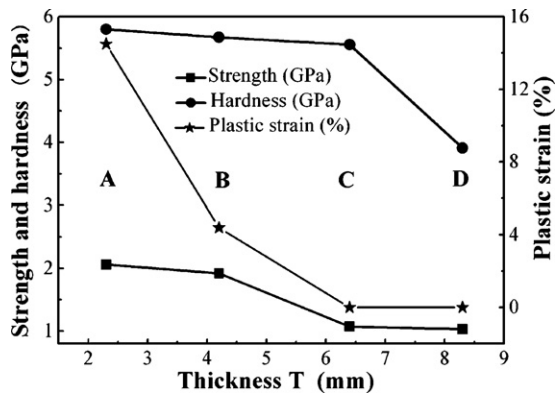


Fig. 3. Curves about the change of uniaxial compressive strength, Vickers hardness and plastic strain with the thickness of as-cast $\text{Cu}_{46}\text{Zr}_{47}\text{Al}_7$ alloys designated samples A–D.

metallic glass matrix. But its plastic strain decreases largely, about by 70%, in comparison with the fully amorphous alloy, implying the plasticity is the most sensitive to the microstructure. For sample C, the hardness still remains relatively high, about 5.4 GPa, slightly smaller than that of sample A or B. But the strength decreases sharply, down to about 1 GPa. This indicates the strength is more sensitive to the microstructure than the hardness. And for the sample D, all mechanical properties decline to the lowest level, controlled by the primary crystallization phases. Besides, in order to further elucidate the relationship between the hardness and strength, the histogram about H_V/σ_b of samples A–D was plotted, as shown in Fig. 4. Apparently, for samples A and B, the values of H_V/σ_b are equal to 2.82 and 2.97, which agree well with the empirical formula $H_V/\sigma_b \approx 3$

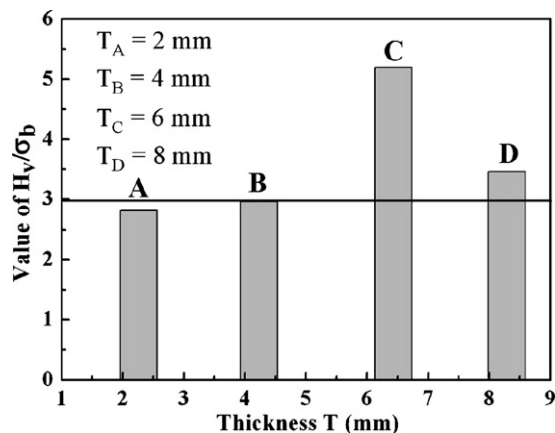


Fig. 4. Relationships between the ratio of Vickers hardness and uniaxial compressive strength (H_V/σ_b) and the constant 3 of the as-cast $\text{Cu}_{46}\text{Zr}_{47}\text{Al}_7$ alloys designated samples A–D.

[20]. But for sample C, the hardness is still very high due to the effect of metallic glass phases, and its strength becomes very low, due to the effect of the abundant emergence of intermetallics and the residual stress, which causes that the value of H_V/σ_b is obviously higher than 3. And for sample D, the completely primary crystallization phases lead to the decrease in the hardness. Thus the value of H_V/σ_b is still quite close to 3. To sum up, for metallic glass composites, the hardness always remains very high due to the effect of metallic glassy matrix, no matter how many volume fractions exist. Whereas the strength is affected by primary crystallization phases, only when their volume fraction is up to large enough and even the plastic strain is very sensitive to the primary crystallization phases, no matter how many volume fractions are. That is, the sensitivity of plasticity, strength and hardness to the microstructure declines one by one. And the empirical formula $H_V/\sigma_b \approx 3$ is very suitable to the fully metallic glass alloy, but it is not well applicable for the BMG composite, especially for the BMG composite with high volume fraction of primary crystallization phases.

3.2. Indentation morphologies of Vickers hardness

Fig. 5 shows the variation of indentation morphologies of samples A–D, respectively. For samples A, B and C [Fig. 5(a)–(c)], the pile-ups can be clearly observed around all the indentations, forming some semi-circular shear bands that seem to emanate from the edge of indentation and propagate in a wavy mode, the same with the report [21]. The size of the pile-ups (i.e., distance from the edge of the indenter imprint to the most outer shear band), δ , is about $4.2 \mu\text{m}$. That seems to be invariable for the three samples, implying that the metallic glassy matrix controls their deformation behavior, corresponding to the similar value of hardness. However, around the indentation of sample D, there is no any trace of shear bands [Fig. 5(d)]. Comparing the four micrographs, another interesting feature is that there are some pleats inside the indentations of samples C and D [Fig. 5(c) and (d)], which might be associated with the local fragmentation and discontinuous deformation process of the brittle primary crystallization phases. However, inside the indentations of samples A and B, the surfaces are very smooth, indicating good and continuous plastic deformation process.

3.3. Deformation and fracture behaviors under small punch tests

The macroscale deformation and fracture morphologies of the samples A–D, subjected to small punch test under the same experiment conditions with the load of 4 kg, are shown in Fig. 6.

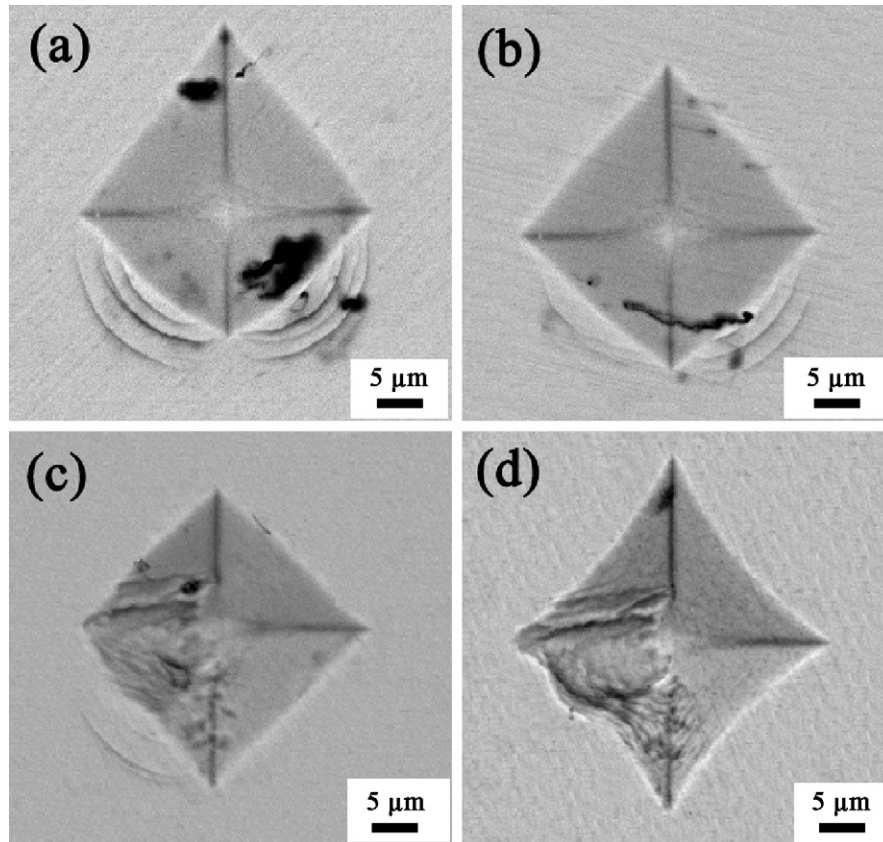


Fig. 5. SEM micrographs showing the surfaces of the as-cast $\text{Cu}_{46}\text{Zr}_{47}\text{Al}_7$ alloys with a mark of indent under a load of 200 g. (a) Sample A, (b) sample B, (c) sample C and (d) sample D.

Apparently, for sample A, due to the isotropic nature of amorphous phase, many radiating shear bands eradiate from the center of the spherical indentation with a proportional spacing, synchronously accompanying with a few secondary shear bands [Fig. 6(a)]. And the total number of the primary shear bands and secondary shear bands is about 32 and 14, indicating that the initial deformation behavior is controlled by the primary shear bands. For sample B, the number of the primary shear bands is about 34, very near to that of sample A. But, the number of secondary shear bands is up to about 66, far more than that of sample A. That indicates that under the same experimental conditions, they show the different plastic deformation ability. Therefore, when applying more loads of 6, 8 and 10 kg to sample A, it can be clearly seen that the sample A can display quite good plastic deformation ability with the highly dense shear bands [Fig. 7(a)–(d)]. In particular, at some local region, the glass flake has been bended to a large degree without fracture, as shown in Fig. 7(c). For better understanding of the shear deformation process, Fig. 8 demonstrates the dependence of the number of shear bands on the applied load. It is interesting to find that both curves climb up very sharply. However, with further increase in the load, the two curves become flat. That illuminates that the number of primary and secondary shear bands rises very slowly, indicating that the two kinds of shear bands have reached to be saturated and then the material will trend to fail when the load is high enough. Meanwhile, it is found that the number of the secondary shear bands is higher than that of primary shear

bands when the applied load is higher than 6 kg, indicating that the secondary shear bands play more important role in the plastic deformation. Under the load of 8 kg, there are also many arc shear bands around the center of spherical indentation, and even some of them circle crookedly into a round [Fig. 7(b)]. At last, under the load of 10 kg, the sample A still failed with partial conglutination, implying sound ductility [Fig. 7(c)]. In addition, it is noted that there are obvious sidesteps whatever along the radial and circumferential directions around the center, indicating a large plastic deformation ability with the formation of multiple shear bands, and the grid pattern was formed on the surface, due to the interaction of the radial and circumferential shear bands [Fig. 7(d)], similar to the report [22].

However, after the small punch test under the load of 4 kg, samples C and D were punched into a hole suddenly in the center of spherical indentation [Fig. 6(c) and (d)], and a small part was broken off from the center of sample D [Fig. 6(d)]. Besides, for sample C, it can be seen that there are still some local shear bands at the tip of cracks in the amplified photos [Fig. 9(a) and (b)]. Those visible shear bands are short and sporadic and are basically parallel to the crack [Fig. 9(b)]. This indicates that local shear deformation can still occur, although sample C has a relatively low strength and zero compressive plastic strain [18]. However, for sample D, it is visible that there is no any shear band, no matter at the tip of local crack or along the crack [Fig. 9(c) and (d)]. In contrast with the sample C, the sample D shows a more brittle fracture feature. Sum up, the small punch

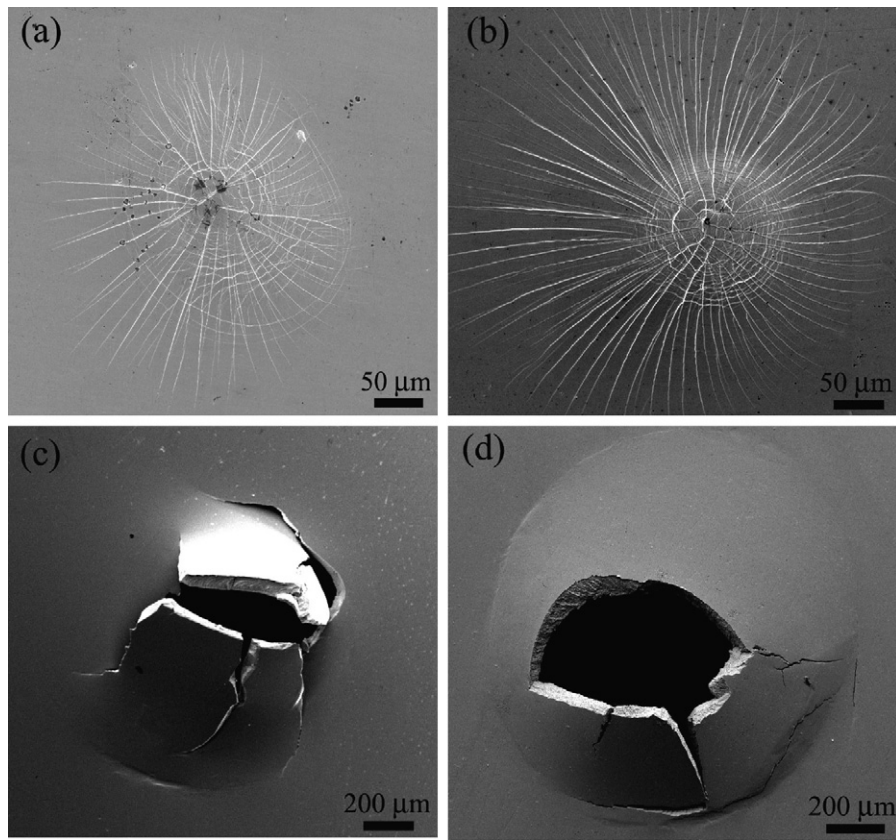


Fig. 6. SEM micrographs showing the surfaces of the as-cast $\text{Cu}_{46}\text{Zr}_{47}\text{Al}_7$ alloys with a mark of small punch test under a load of 4 kg and 0.5 mm diameter of the spherical indenter. (a) Sample A, (b) sample B, (c) sample C and (d) sample D.

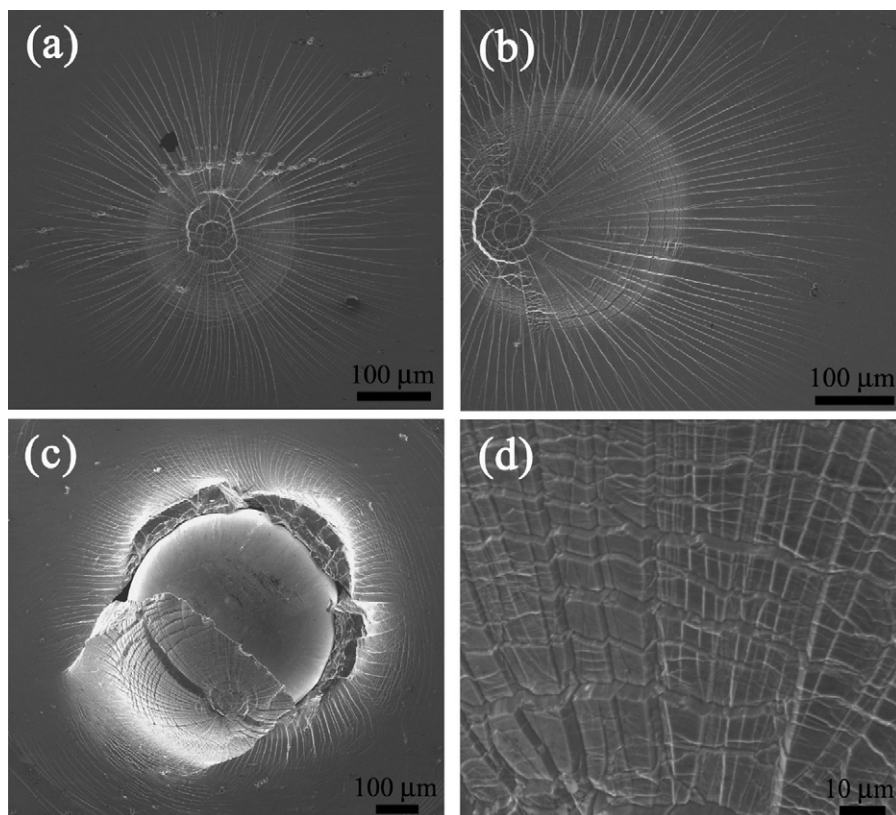


Fig. 7. SEM micrographs showing the surfaces of sample A, with a mark of small punch test under different load: (a) 6 kg, (b) 8 kg, (c) 10 kg and (d) 10 kg.

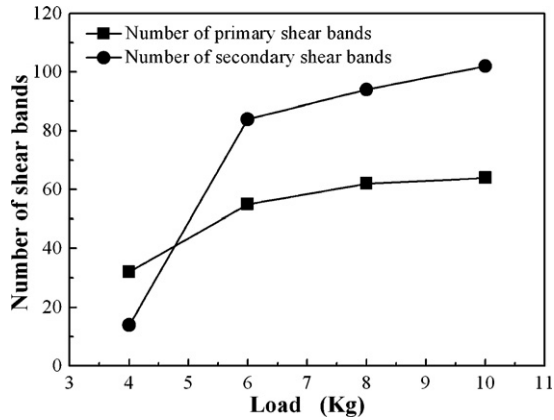


Fig. 8. The changes of the number of shear bands with the load under the punch test of sample A.

test can more elaborately characterize the formation and evolution of shear bands and also more effectively distinguish the intrinsic shear deformation ability for the brittle metallic glass composites.

3.4. Ductile to brittle transition

As is well known, for the brittle materials, the compressive failure is always controlled either by the Tresca criterion or by the Mohr–Coulomb criterion [23–26]. And for the compressive

failure of the Zr-based BMG composite, due to the effect of the normal stress, the Mohr–Coulomb criterion should be more suitable to describe the critical compression failure condition, i.e.

$$\tau_n = \tau_0 + \mu\sigma_n \tag{2}$$

where τ_n is the critical shear fracture stress, τ_0 the intrinsic shear strength and μ is the material constant. This expression can be illustrated in Fig. 10. When the ductile metallic glass composite fails in a shear mode [27], the critical fracture line corresponds to the line SE in Fig. 10(a). And when some brittle metallic glass composites or ceramics fail in a splitting or fragmentation mode [28,29], the critical fracture line corresponds to the line DE in Fig. 10(a). In this case, it was proposed that there is a critical distensile fracture stress, σ_D , leading to the distensile or splitting fracture of the materials, illustrated by the line DE in Fig. 10(a), which strongly depends on the intrinsic cleavage stress, σ_0 . Generally, when the intrinsic cleavage stress, σ_0 , decreases, the distensile fracture stress, σ_D , will decrease too and the distensile fracture line DE will move towards to the negative direction of the stress axis, just as the fracture behaviors of $\text{Al}_2\text{O}_3/\text{Nb}/\text{Al}_2\text{O}_3$ composites [28] and Ti-based composites [29].

According to the Mohr–Coulomb criterion and the compressive stress Mohr circle, when the critical distensile fracture stress, σ_D , is higher than the critical shear fracture stress, σ_C^F ,

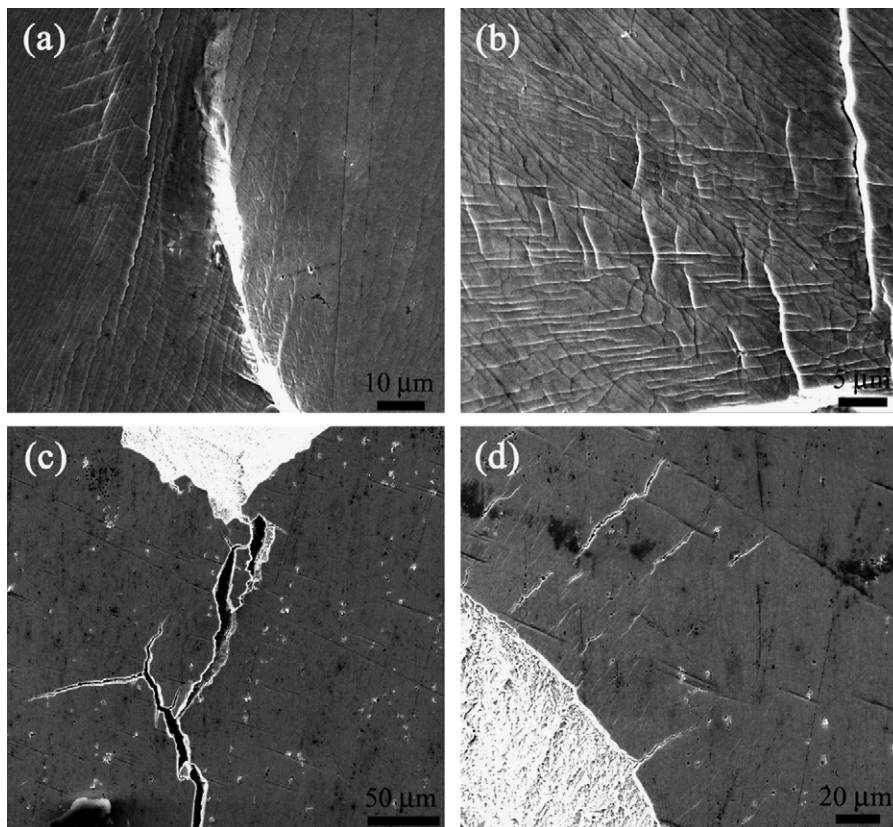


Fig. 9. SEM micrographs showing the fractured surfaces of samples C and D under the small punch test with a load of 4 kg and the spherical indenter in 0.5 mm diameter: (a) and (b) sample C; (c) and (d) sample D.

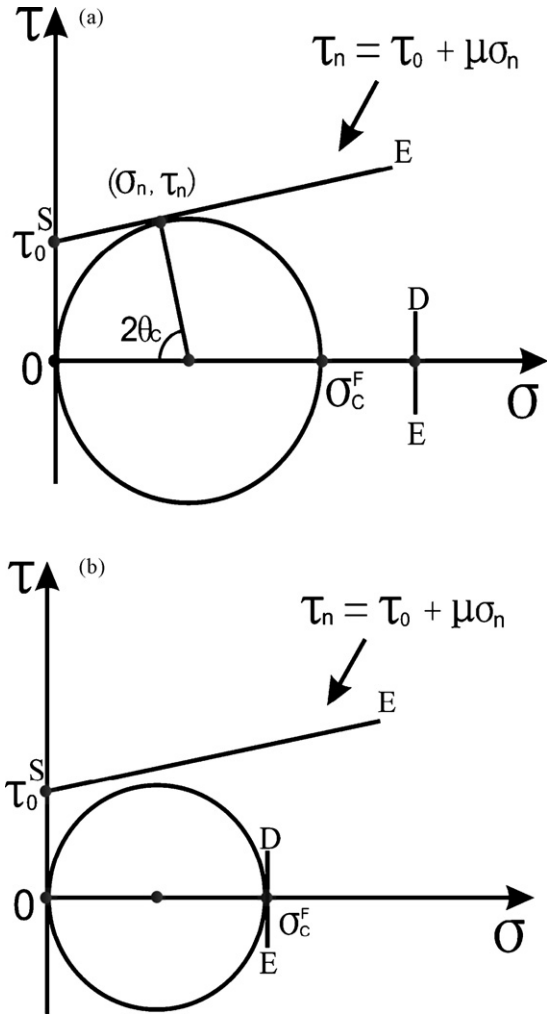


Fig. 10. Illustration of (a) critical compressive fracture condition of shear fracture mode and (b) the condition of distensile fracture mode.

i.e., $\sigma_D > \sigma_C^F$, the stress Mohr circle will first touch the shear fracture line SE. In this case, the material will fail in a shear mode [Fig. 10(a)]. On the contrary, when the critical distensile fracture stress, σ_D , is smaller than the critical shear fracture stress, σ_C^F , i.e., $\sigma_D < \sigma_C^F$, the stress Mohr circle will first touch the distensile fracture line DE [Fig. 10(b)]. Therefore, the specimen will fail in a distensile mode, displaying a local crack rather than macroscopic shear crack [28,29]. The final failure mode of a BMG composite is always a competitive process among shear, distensile and split fracture [29]. In essence, the competitive process should depend on the ratio:

$$\alpha = \frac{\tau_0}{\sigma_0} \quad (3)$$

where τ_0 is the intrinsic shear strength and σ_0 is the intrinsic cleavage strength [30].

For the currently studied BMG composites, sample A has an extremely high-compressive fracture strength, which should correspond to high-intrinsic shear strength, τ_0 [18,30]. Also, it is deduced that the intrinsic cleavage strength, σ_0 , must be quite high, which leads to a low ratio, $\alpha = \tau_0/\sigma_0$, so the dense shear bands are easily formed [Fig. 7(c) and (d)]. Therefore,

the sample A only failed in a shear mode with a high-plastic strain. In a word, for sample A, its intrinsic shear strength, τ_0 , and intrinsic cleavage strength, σ_0 , must match well with a low ratio, $\alpha = \tau_0/\sigma_0$ [30], so that it often deforms and fails in a shear mode, together with high strength and good plasticity.

On the other hand, for the BMGs composites, since the multifarious fracture mechanisms can be attributed to the effect of primary crystallization phases, the physical meaning of the constant, $\alpha = \tau_0/\sigma_0$, must reflect the intrinsic character of the microstructure. Whether the distensile fracture occurs or not depends on the ratio, $\alpha = \tau_0/\sigma_0$, responding to the results of the interactions between the primary crystallization phases and the matrix of the composites [10,12,31–33]. Therefore, for sample B, the activation of fewer shear bands [Fig. 6(b)] and the low plasticity (Table 1) manifest the slight increase in the ratio, $\alpha = \tau_0/\sigma_0$. So the distensile fracture line DE might move towards the negative axis to some extent, but the stress Mohr circle still first touches shear fracture line SE, and the sample failed in a shear mode with high-fracture strength.

In addition, for samples C and D, due to the intensive effect of many primary crystallization phases, their intrinsic cleavage strength, σ_0 , decreases sharply. Thus, the ratio, $\alpha = \tau_0/\sigma_0$ should greatly increase, compared with samples A and B, deducing from nearly no macroscopic shear bands on the surface [Fig. 6(c) and (d)]. Besides, due to the low-intrinsic cleavage strength, σ_0 , the distensile fracture line DE will move largely towards the negative stress axis. So that the stress Mohr circle first touches the distensile fracture line DE, and they failed in a distensile or split fracture mode, indicating by the cracks [Fig. 6(c) and (d)]. Since the ratio, $\alpha = \tau_0/\sigma_0$, increases, it is hard for the samples C and D to deform in a shear mode and form multiple interacting shear bands. On the contrary, they had to fail in a cleavage fracture mode with zero plasticity and low-fracture strength.

Finally, for sample C, it is worthy noting that there is no any shear band activated under compressive loading [18], however, some short shear bands were still activated under the Vickers hardness [Fig. 5(c)] and small punch test [Fig. 9(a) and (b)], indicating that the actual failure mode and the activation of shear bands depend on the loading mode to some extent. But for sample D, no shear band was triggered, no matter whether subjected to Vickers indentation or small punch test. This indicates that there is still some difference in the shear deformation ability between samples C and D, although they displayed quite similar properties under conventional compression test [18]. The small punch tests give a clear evidence about the local activation of shear bands in sample C [Fig. 9(a) and (b)], and no shear band appearance in sample D [Fig. 9(c) and (d)]. Furthermore, it is suggested that the small punch test can be regarded as an effective method to distinguish the shear deformation ability and ductile to brittle transition in different brittle metallic glass composites.

4. Conclusions

1. For $\text{Cu}_{46}\text{Zr}_{47}\text{Al}_7$ (at.%) alloy, it is found that the mechanical properties are very sensitive to the microstructures with different volume fraction of primary crystallization phases,

with a ductile to brittle transition behavior. Furthermore, the Vickers hardness will decline notably, only when the metallic glass matrix disappears completely; however, the strength will decline when the volume fraction of primary crystallization phases is high enough (about >30%); the plasticity will decline, once the primary crystallization phases precipitate.

2. Except for the conventional Vickers hardness test, the small punch test can be introduced as a new experimental method to trigger successfully the formation and propagation of shear bands in different metallic glass composites. For the fully amorphous sample and the sample with few primary crystallization phases, the dense multiple shear bands can be activated even to form a grid pattern after small punch tests. And even, for those brittle metallic glass composites, the small punch test can also successfully distinguish the difference in their intrinsic shear deformation ability.

Acknowledgements

The authors would like to thank W. Gao and F.F. Wu for mechanical tests and SEM observations. This work is financially supported by the National Natural Science Foundation of China (NSFC) under Grant Nos. 50401019 and 50501017, the “Hundred of Talents Project” by Chinese Academy of Science and the National Outstanding Young Scientist Foundation for Z.F. Zhang under Grant No. 50625103.

References

- [1] A.J. Drehman, A.L. Greer, D. Turnbull, *Appl. Phys. Lett.* 41 (1982) 716–717.
- [2] Y.J. Kim, R. Busch, W.L. Johnson, A.J. Rulison, W.K. Rhim, *Appl. Phys. Lett.* 65 (1994) 2136–2138.
- [3] A. Inoue, T. Zhang, *Mater. Trans. JIM* 37 (1996) 185187.
- [4] W.L. Johnson, *Curr. Opin. Solid State Mater. Sci.* 1 (1996) 383–386.
- [5] Z.F. Zhang, J. Eckert, L. Schultz, *Acta Mater.* 51 (2003) 1167–1479.
- [6] J.F. Löffler, *Intermetallics* 11 (2003) 529–540.
- [7] W.H. Wang, C. Dong, C.H. Shek, *Mater. Sci. Eng. R* 44 (2004) 45–89.
- [8] G. He, Z.F. Zhang, W. Loser, J. Eckert, L. Schultz, *Acta Mater.* 51 (2003) 2383–2395.
- [9] J. Eckert, G. He, J. Das, W. Loser, *Mater. Trans.* 44 (2003) 1999–2006.
- [10] C.C. Hays, C.P. Kim, W.L. Johnson, *Phys. Rev. Lett.* 84 (2000) 2901–2904.
- [11] H. Kato, T. Hirano, A. Matsuo, Y. Kawamura, A. Inoue, *Scr. Mater.* 43 (2000) 503–507.
- [12] C. Fan, R.T. Ott, T.C. Hufnagel, *Appl. Phys. Lett.* 81 (2002) 1020–1022.
- [13] J. Das, M.B. Tang, K.B. Kim, R. Theissmann, F. Baier, W.H. Wang, J. Eckert, *Phys. Rev. Lett.* 94 (2005) 205501.
- [14] Y.F. Sun, B.C. Wei, Y.R. Wang, W.H. Li, T.L. Cheung, C.H. Shek, *Appl. Phys. Lett.* 87 (2005) 051905.
- [15] A. Kawashima, H. Kurishita, H. Kimura, T. Zhang, A. Inoue, *Mater. Trans.* 46 (2005) 1725–1732.
- [16] F. Jiang, Z.J. Wang, Z.B. Zhang, J. Sun, *Scr. Mater.* 53 (2005) 487–491.
- [17] J. Eckert, J. Das, K.B. Kim, F. Baier, M.B. Tang, W.H. Wang, Z.F. Zhang, *Intermetallics* 14 (2006) 876–881.
- [18] J.T. Fan, F.F. Wu, Z.F. Zhang, F. Jiang, J. Sun, S.X. Mao, *J. Non-Cryst. Solids*, (2007) in press.
- [19] Z. Bian, H. Kato, C.L. Qin, W. Zhang, A. Inoue, *Acta Mater.* 53 (2005) 2037–2048.
- [20] A. Stoica, J. Eckert, S. Roth, Z.F. Zhang, L. Schultz, W.H. Wang, *Intermetallics* 13 (2005) 764–769.
- [21] U. Ramamurty, S. Jana, Y. Kawamura, K. Chattopadhyay, *Acta Mater.* 53 (2005) 705–717.
- [22] F.F. Wu, Z.F. Zhang, F. Jiang, J. Sun, J. Shen, S.X. Mao, *Appl. Phys. Lett.* 90 (2007) 191909.
- [23] M.H. Yu, A Book, Springer, Berlin, Germany, 2001.
- [24] Z.F. Zhang, G. He, J. Eckert, L. Schultz, *Phys. Rev. Lett.* 91 (2003) 045505.
- [25] J.J. Lewandowski, P. Lowhaphandu, *Philos. Mag. A* 82 (2002) 3427–3441.
- [26] C.A. Schuh, A.C. Lund, *Nat. Mater.* 2 (2003) 449–452.
- [27] Y.C. Kim, W.T. Kim, D.H. Kim, *Mater. Sci. Eng. A* 375–377 (2004) 127–135.
- [28] Z.F. Zhang, D. Brunner, C. Scheu, M. Rühle, *Z. Metallk.* 96 (2005) 62–70.
- [29] Z.F. Zhang, G. He, J. Eckert, *Philos. Mag.* 85 (2005) 897–915.
- [30] Z.F. Zhang, J. Eckert, *Phys. Rev. Lett.* 94 (2005) 094301.
- [31] R.D. Conner, R.B. Dliker, W.L. Johnson, *Acta Mater.* 46 (1998) 6089–6102.
- [32] F. Szeucs, C.P. Kim, W.L. Johnson, *Acta Mater.* 49 (2001) 1507–1513.
- [33] G. He, J. Eckert, W. Loser, L. Schultz, *Nat. Mater.* 2 (2003) 33–37.